Hydrogen wettability and capillary pressure in Clashach sandstone for underground hydrogen storage

*Eike M. Thaysen[1,2], Zaid Jangda[3], Aliakbar Hassanpouryouzband[1], Hannah Menke[3], Kamaljit Singh[3], Ian B. Butler[1], Niklas Heinemann[1], Katriona Edlmann[1]*

[1]School of Geoscience, Grant Institute, The King's Buildings, The University of Edinburgh, James Hutton Road, Edinburgh, EH9 3FE, United Kingdom

[2]Department of Geosciences, Institute of Environmental Assessment and Water Research (IDAEA), Severo Ochoa Excellence Center of the Spanish Council for Scientific Research (CSIC), Jordi Girona 18–26, 08034 Barcelona, Spain

[3]Institute of GeoEnergy Engineering, Heriot-Watt University, EH14 4AS, Edinburgh, UK

# Hydrogen wettability and capillary pressure in Clashach sandstone for underground hydrogen storage

*Eike M. Thaysen[1,2], Zaid Jangda[3], Aliakbar Hassanpouryouzband[1], Hannah Menke[3], Kamaljit Singh[3], Ian B. Butler[1], Niklas Heinemann[1], Katriona Edlmann[1]*

[1]School of Geoscience, Grant Institute, The King's Buildings, The University of Edinburgh, James Hutton Road, Edinburgh, EH9 3FE, United Kingdom

[2]Department of Geosciences, Institute of Environmental Assessment and Water Research (IDAEA), Severo Ochoa Excellence Center of the Spanish Council for Scientific Research (CSIC), Jordi Girona 18–26, 08034 Barcelona, Spain

[3]Institute of GeoEnergy Engineering, Heriot-Watt University, EH14 4AS, Edinburgh, UK

19     ABSTRACT

20     To meet global commitments to reach net-zero carbon (C) emissions by 2050, the energy mix

21     must be adjusted to reduce emissions from fossil fuels and transition to low or zero C energy

22     sources. Hydrogen ($H_2$) can support this transition by facilitating increased renewable (zero C)

23     energy use by acting as an energy store to balance supply and demand. Underground $H_2$ storage

24     in porous media is investigated due to its high capacity and economical price. An important

25     unknown in underground porous media $H_2$ storage is the volume of recoverable $H_2$ which is

26     partly controlled by the $H_2$ wettability.

27     We computed receding and advancing contact angles for the $H_2$-brine-Clashach sandstone

28     system at pore fluid pressures of 2-7 MPa and for nitrogen ($N_2$)-brine-Clashach sandstone at 5

29     MPa, based on X-ray microtomography images of gas displacement and trapping in Clashach

30     sandstone. A centrifuge analysis of the capillary pressure ($P_c$) at varying water saturations was

31     conducted for $N_2$. The $H_2$ $P_c$ curve was derived from the $N_2$ $P_c$, the $N_2$ wettability

32     measurements, and existing information on the density differential and the interfacial tensions

33     between brine and $H_2$ and $N_2$, respectively.

34     The results show no change of the $H_2$-brine-Clashach sandstone contact angles within the

35     examined pressure range, with mean receding (drainage) and advancing (imbibition) contact

36     angles of 61°± 24-26° and 58°± 20-22°, respectively, at all pore fluid pressures, indicating a

37     water-wet rock and that increased hydrogen residual trapping at higher pressure was not

38     controlled by wettability. $N_2$-brine-Clashach sandstone receding and advancing contact angles

39     were 66°± 21° and 62°± 24°, respectively. We found $H_2$ $P_c$ of 0.43 MPa at irreducible water

40     saturations of 12.6-14.0%. Our results provide detailed insights into the controls on $H_2$
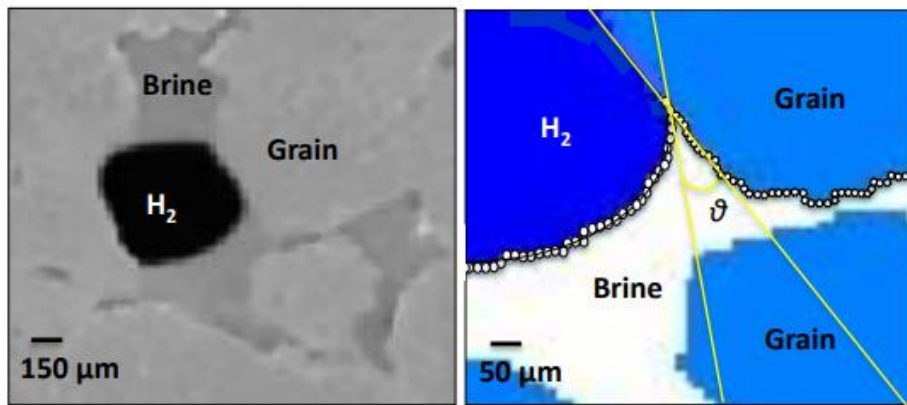
41    displacement and capillary trapping as well as crucial input parameters for the modelling and

42    design of $H_2$ storage operations in porous media.

43

44    KEYWORDS Hydrogen, underground storage, µCT, wetting state, capillary pressure, flow

45    experiments, nitrogen

46

47    GRAPHICAL ABSTRACT

48    

49

## 1. INTRODUCTION

Climate change is a major problem of increasing global relevance that will have wide ranging adverse implications for all life on Earth [1, 2]. In order to mitigate climate change we must reduce our reliance on fossil fuels, which currently account for over 75% of our greenhouse gas emissions, reduce atmospheric carbon dioxide ($CO_2$) concentrations and transition to a low carbon (C) society [1]. This requires the implementation of passive and active $CO_2$ sequestration technologies (e.g., [3-5]), and an increase in the proportion of renewable energy such as wind and solar energy into the near future. A major challenge for renewable energy is the imbalance between supply and demand [6]. A way of overcoming this imbalance is the generation of $H_2$ via electrolysis of water during periods of renewable energy oversupply with subsequent underground $H_2$ storage [7, 8] that allows for recovery and use of $H_2$ as an energy source during periods of renewable energy shortage. Electricity generation from stored $H_2$ could balance seasonal electricity demands, yet the low energy density of $H_2$ requires large-scale storage capacities that are only available in geological media [9]. While underground storage of $H_2$ in salt caverns plays an important part in the daily and weekly reduction of energy imbalances, seasonal balancing may only be achieved with $H_2$ storage in underground porous media including depleted gas fields and saline aquifers that have TWh storage capacities [9, 10].

Emerging evidence suggests there are no important showstoppers for the implementation of porous media $H_2$ storage [11-19]. Yet, certain knowledge gaps remain to be addressed, amongst them the $H_2$ fluid flow behavior in the porous medium, which, along with the injected cushion gas, governs gas injectivity and recovery from the reservoir [9, 20]. Of particular importance for describing the $H_2$ fluid flow in the porous medium is the determinations of capillary pressure and relative permeability [21] as well as quantification of $H_2$ saturation and trapping inside rocks, which can be achieved through pore-scale visualization studies [22]. These factors

75  directly relate to the fluids present inside the porous medium and inform simulation models to

76  predict $H_2$ displacement and trapping and upscaling to the reservoir scale.

77      The key parameter for controlling multiphase fluid flow in porous media is wettability [23].

78  Wettability is characterized as the spatial distribution of the contact angle at the contact line

79  between two fluids and the solid matrix. It is measured through the densest fluid, with a contact

80  angle of 0 reflecting a perfectly wetting fluid  [24, 25]. Wettability influences flow dynamics

81  such as relative permeability, $P_c$ and irreducible water saturation, all of which in turn are

82  influenced by the pore network morphology, connectivity and tortuosity. Accurate knowledge

83  of wettability over geological conditions (e.g. rock mineralogy, brine composition, pressure,

84  temperature) is key for the design and optimization of $H_2$ storage projects [26].

85      Recent investigations of $H_2$ contact angles in quartz or sandstone report ranges of 5° to 60°

86  [16, 22, 27-32], depending on the measurement methodology, the experimental conditions and

87  whether hysteresis was studied. Notably, there is an apparent discrepancy in the published

88  studies on $H_2$ contact angles. While Hashemi et al. [28] and Higgs et al. [27] reported contact

89  angles of 25-45° in Bentheimer and Berea sandstones without meaningful pressure or

90  temperature correlations of the contact angle (captive-bubble method, 0.7-10 MPa and 20-50

91  °C), Iglauer et al. [31] reported an increase of $H_2$/brine/quartz contact angles of 10-15° with a

92  pressure increase from 10 to 15 MPa using the tilted plate method.

93      Similar discrepancies are also found in $H_2$ relative permeabilities studies. Rezaei et al. [17]

94  showed that shallower i.e. lower pressure sites are recommended for future $H_2$ storage

95  operations in porous media due to a reduced relative permeability at higher $H_2$ saturations and

96  high pressures of 10.7-20.7 MPa (unsteady state method, vertical core). This contrasts with

97  previous findings by Yekta et al. [29] who documented little change of the $H_2$ relative

98  permeability at pressure increases from 5.5 MPa to 10 MPa using the steady state technique.

99  In addition, Rezaei et al. [17] showed good similarity between $H_2$ and $N_2$ relative permeability

100 curves, while Lysyy et al. [33], Al-Yaseri et al. [34] and Zhang et al. [32] report divergent

101 displacement behavior of $H_2$ and $N_2$. Thaysen et al. [11] reported similar displacement behavior

102 of $H_2$ and $N_2$ during drainage but the residual saturation after imbibition, $S_{nwr}$, was much higher

103 for $N_2$.

104   In this work, we used previously acquired X-ray microtomography ($\mu CT$) images of $H_2$ and

105 brine core-flood experiments in a Clashach sandstone at 2-7 MPa pore fluid pressure and

106 ambient temperature (293 K) [11] to determine *in-situ* macroscopic $H_2$/brine/Clashach

107 sandstone contact angles after drainage, $\theta_{receding}$, and imbibition, $\theta_{advancing}$, and hence, to identify

108 a possible control of wettability on the $H_2$ injectivity and recovery. We hypothesized that

109 $\theta_{advancing}$ would decrease with increasing pore fluid pressure, corresponding to previous

110 observations of increased trapping at higher pressure [11]. Using $\mu CT$-images of $N_2$ and brine

111 core-flood experiments in a Clashach sandstone at 5 MPa, we further quantified

112 $N_2$/brine/Clashach sandstone contact angles. Measurements of the $P_c$ at varying brine saturation

113 for $N_2$ were conducted and results were combined with the $N_2$ wettability during drainage, as

114 well as with existing information on the density differential and the interfacial tensions between

115 brine and $H_2$ and $N_2$, to calculate the $H_2$ $P_c$. We show that, for the same rock sample, the

116 $\theta_{advancing}$ did not change with pore fluid pressure, indicating that, based on the wettability alone,

117 no change in $H_2$ trapping with increasing pressure is expected. This work pioneers a high-

118 precision $H_2$ capillary pressure curve for Clashach sandstone with $H_2$ $P_c$ of 0.43 MPa at

119 irreducible water saturations of 12.6-14.0%. The aim of this study is to provide detailed insights

120 into the controls on $H_2$ movement, displacement and capillary trapping. Our results may serve

121 to inform the basic models for appropriate understanding of gas storage operations, as well as

122 to influence their designs and predictions.

123

124 2. MATERIALS AND METHODS

125 *2.1 Core Flood Experiments*

126   Two-phase non-steady core flooding experiments at 2-7 MPa pore fluid pressure and ambient

127 temperature (~293 K) by Thaysen et al. [11] were used as input data for this wettability study.

128 In short, the $H_2$ (purity 99.9995 vol.%, BOC Ltd.) and brine (0.5 M CsCl, Sigma-Aldrich)

129 injections used the same untreated Clashach sandstone outcrop sample of 4.7 mm diameter and

130 a length of 57 mm (Clashach composition: ~96 wt.% quartz, 2% K-feldspar, 1% calcite, 1%

131 ankerite [35], porosity 11.1-14.4% [35-37]). For all experiments, the same water-wet Clashach

132 sandstone plug was first saturated with brine at a flow rate of 70 µl min$^{-1}$. Afterwards, $H_2$ was

133 injected (drainage) into the brine-saturated Clashach sandstone plug at a flow rates of 20 µl

134 min$^{-1}$, based on desired capillary-regime capillary numbers, $N_C$, of $1.7 \times 10^{-8}$ (The viscosity of

135 $H_2$ is 9.01 µPa s at 298 K and 4.7 MPa [38] and the IFT between $H_2$ and water is 72.6 mN m$^{-1}$

136 at 298 K and 5 MPa [39, 40]). Subsequently, brine was reinjected (imbibition) at a flow rates

137 of 20 µl min$^{-1}$, resulting in $N_C$ of $2.4 \times 10^{-6}$ (using the same IFT between $H_2$ and water of 72.6

138 mN m$^{-1}$ at 5 MPa and 298 K [39, 40] and a viscosity of $1.07 \times 10^{-3}$ Pa s for 0.6 M KI and 293 K

139 [35]). One experiment at 5 MPa and 298 K used $N_2$ instead of $H_2$. The $N_C$ of the $N_2$ experiment

140 was $3.5 \times 10^{-8}$ (using an IFT of 73 mN m$^{-1}$ between $N_2$ and water at 298 K and 10 MPa [41] and

141 a viscosity of $1.89 \times 10^{-5}$ Pa s at 5 MPa and 295 K [38]). At the end of each experiment (one

142 drainage and imbibition cycle), the Clashach sandstone sample was depressurized, following

143 reinjection of brine to ensure that all $H_2$ was removed from the core to prepare for subsequent

144 experiments. 3D volumes were acquired with µCT from the lower central portion of the sample

145 at the end of each injection step (ten pore volumes). Images were processed as described in

146 Thaysen et al. [11].

147

148 *2.2 Wettability Analysis*

149    The wettability was characterized for one of each duplicate $H_2$ experiment carried out at 2, 5

150    and 7 MPa (see asterisks in Fig. 1) and for the $N_2$ experiment (Fig. 1g) by measuring the

151    gas/brine/Clashach sandstone contact angles on each voxel at the three-phase contact line on a

152    sub-volume of 500 $\mu m^3$ using a highly accurate, widely-applied algorithm for automatic

153    contact angle measurement of µCT-images [42]. The algorithm identifies and meshes the

154    interfaces throughout the segmented stack of images and then reduces noise and imposes a

155    constant curvature by smoothing the data. Subsequently, two normal vectors are placed at each

156    contact point and the dot product of these vectors (where they meet at the contact line) is used

157    to determine the contact angle at each contact point along the contact line [42]. Data dispersion

158    in contact angle measurements was calculated as the standard deviations of the mean.

159

160    *2.3 Hydrogen Capillary Pressure ($P_{cH2}$)*

161    The capillary pressure with air displacing brine, using $N_2$ as a proxy, was determined using

162    the high-speed centrifuge method [43] on two Clashach core plugs that were drilled from the

163    same outcrop rock as the one sample used for the core flood experiments (see Supporting

164    Information (SI) for method details). A comprehensive description of the $P_c$ measurement for

165    air is provided in the SI Text S1. To compute the $P_{cH2}$ from the air $P_c$, we employed the recently

166    published conversion factor, $\psi N_2/H_2$ (Eq. 1) [44]:

167    $$\Psi_{N_2/H_2} = \frac{\Delta\rho_{N_2/water}}{\Delta\rho_{H_2/water}} \frac{\gamma_{H_2/water}}{\gamma_{N_2/water}} \frac{\cos\theta_{H_2/water}}{\cos\theta_{N_2/water}} \qquad (1)$$

168    where $\Delta\rho_{N2/water}$ and $\Delta\rho_{H2/water}$, represent the density differential between the gases and saline

169    water under reservoir conditions. Brine density was deduced using the Danesh method [45].

170    The terms $\gamma_{N2/water}$ and $\gamma_{H2/water}$, denote the interfacial tension (IFT) between the gases and water

171
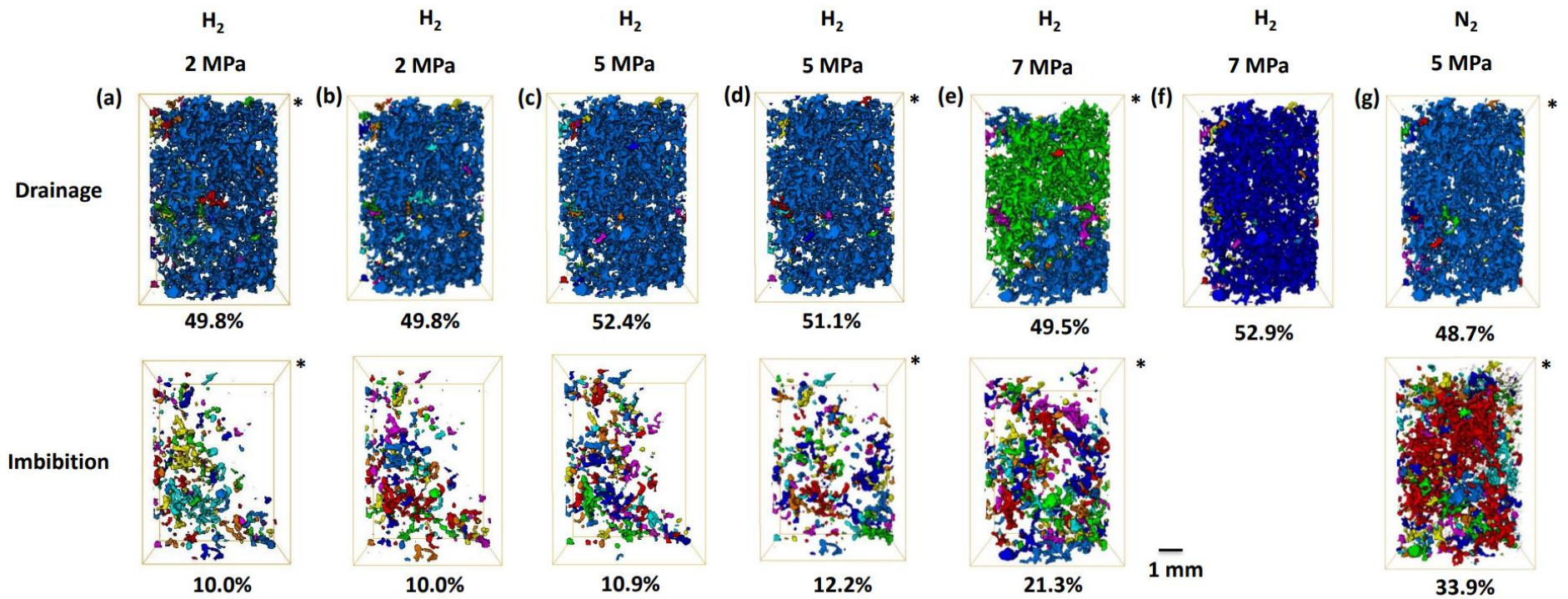
Figure 1. 3D renderings of gas clusters with gas saturation percentages in the pore space after drainage and primary imbibition at 2-7 MPa. Discrete clusters were rendered in colors, where mainly one color marks one large, connected cluster and different colors indicate several, not connected clusters. (a-b) $H_2$ at 2 MPa, (c-d) $H_2$ at 5 MPa and (e-f) $H_2$ at 7 MPa, (g) $N_2$ at 5 MPa, all at a constant flow rate of 20 µl min$^{-1}$. Asterisks mark data utilized for the contact angle analysis. Adapted from Thaysen et al. [11].

176     and made use of the methodology for calculation of the IFT by Meybodi et al. [46], as

177     previously detailed [44]. The last terms, $cos\theta_{N2/water}$ and $cos\theta_{H2/water}$, represent the wettability of

178     the Clashach sandstone samples. With this conversion factor in place, the $P_{cH2}$ at varying water

179     saturations is ascertained by Eq. 2

180 $$Pc_{H_2} = \Psi_{N_2/H_2} \times Pc_{N_2} \tag{2}$$

181     All parameters used to calculate the $\psi N_2/H_2$ and $P_{cH2}$ are provided in SI Table 2.

182

183

184     3 RESULTS

185     *3.1 H₂-brine-Clashach sandstone contact angles relative to H₂ pore space saturations*
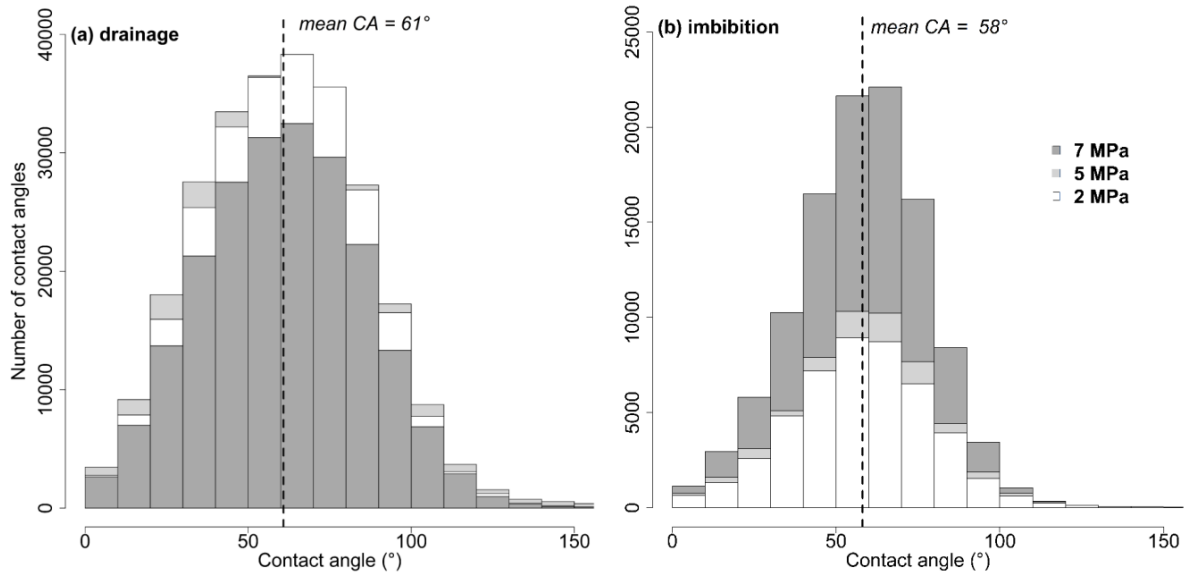
186     Hydrogen-brine-Clashach sandstone contact angles were normally distributed and showed

187     $\theta_{receding}$ of 61.09°, 61.01° and 60.82° at 2, 5 and 7 MPa pore fluid pressure, with standard

188     deviations of 24°, 26° and 24°, respectively (Fig. 2a). $\theta_{advancing}$ were $57.8 \pm 21°$, $58.1 \pm 22°$ and

189     $57.8 \pm 20°$ at 2, 5 and 7 MPa pore fluid pressure, respectively (Fig. 2b). Initial H₂ saturation

190     was~50% at all pore fluid pressures (Fig. 1). Trapped H₂ in the pore space after imbibition

191     increased from 10-12% at 2-5 MPa to 21% at 7 MPa (Fig. 1), with a significant cluster build-

192     up at 7 MPa (Fig. 1e). The total mass of trapped H₂ at 2, 5 and 7 MPa, considering saturation

193     and density differences with pressure, was 0.022 mg, 56.3-67.6 mg and 165.6 mg, respectively.

194

195     *3.2 N₂-brine-Clashach sandstone contact angles relative to N₂ pore space saturations*

196     Nitrogen-brine-Clashach sandstone contact angles were normally distributed and were 66.5°

197     $\pm 21°$ and $62.1° \pm 24°$ after drainage and imbibition, respectively, at 5 MPa pore fluid pressure

198

Figure 2. Drainage (a) and imbibition (b) contact angle distributions measured at the H$_2$/brine/Clashach sandstone interface at 2, 5 and 7 MPa pore fluid pressure. Note the different y-axes scales. The number of contact angles in these graphs is proportional to the H$_2$ saturation in the pore space. During drainage, a mean contact angle of 61° was observed at all pressures and H$_2$ saturation in the pore space was similar. During imbibition, the mean contact angle was 58° at all pore fluid pressures and a larger volume of H$_2$ was trapped at 7 MPa relative to at lower pressures.


(Fig. 3). Initial and residual saturations of N$_2$ were 49% and 34%, respectively (Fig. 1g).


*3.3 P$_c$ and irreducible water saturation*

Figure 4 shows the drainage $P_c$ curve for H$_2$ for two Clashach sandstone plugs with permeabilities of 139 mD and 178 mD, respectively. Under ambient conditions, $P_{cH2}$ is approximately 1.3 to 1.36 times greater than that of N$_2$ (SI Table S2). The most pronounced impact on $P_c$ stems from differences in wettability, contributing to approximately 19% of the effect (SI Table S2). The IFT and density differential between H$_2$ and N$_2$ relative to brine

216 contribute less to the differences in $P_c$, as IFT for both $H_2$ and $N_2$ exhibit a variation of less than

217 8% and the density differential is less than 3% (SI Table S2). The irreducible water saturation

218 of Clashach sandstone is 12.6-14% and is reached at 0.43 MPa and 0.35 MPa for $H_2$ and $N_2$,

219 respectively (Fig. 4, SI Table S2).

220

221 4. DISCUSSION

222 *4.1 $H_2$-brine-Clashach sandstone contact angles*

223 We observed normal distributions of $\theta_{receding}$ and $\theta_{advancing}$ (Fig. 2). If the solid surface was

224 truly smooth and mineralogically homogeneous, all contact angles would be identical. The pore

225 walls of naturally occurring rocks however are characterized by a certain surface roughness

226 and mineralogical

227 heterogeneity; hence,

228 contact angles in real rock

229 samples show some scatter,

230 creating a distribution of

231 contact angles [24]. In

232 addition, the voxel size of

233 5.4 um$^3$ of the μCT images

234 implies an inability to

235 completely resolve the
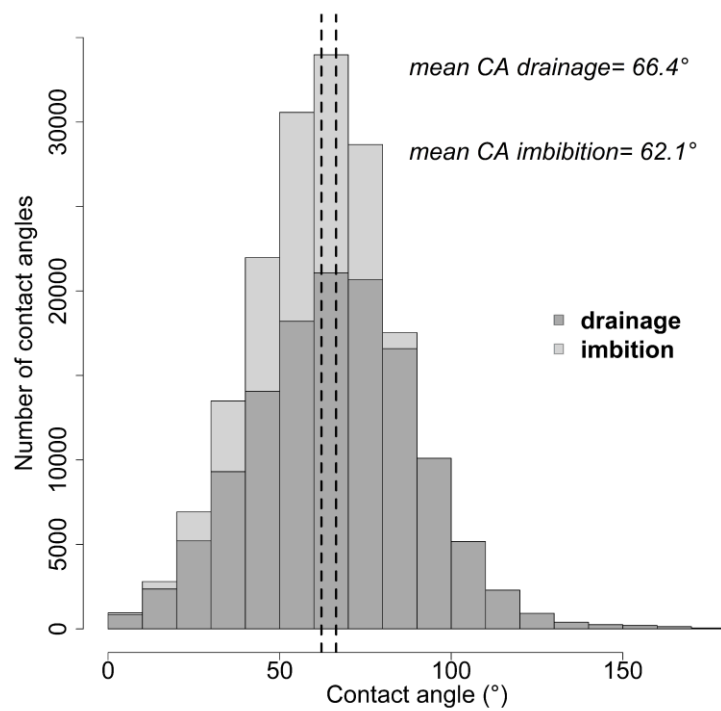
236 three-phase contact line

237 which could cause

238 segmentation errors and

239 contact angle measurement

240 errors, contributing to the



Figure 3. Contact angle distributions at the $N_2$/brine/Clashach sandstone interface after drainage and imbibition at 5 MPa pore fluid pressure showing average contact angles of 66° and 62°, respectively.

241  observed large range of contact angles. Resolution limitations on contact angle measurements

242  manifest in particular during drainage when the saturation of the nonwetting phase increases

243  and the fluid-fluid interfaces move into the pore throats where the voxel count is limited [47].

244  Considering standard

245  deviations of 20-26% in the

246  $H_2$ contact angle

247  measurements, the mean

248  drainage and imbibition

249  contact angles of 61° and 58°,

250  respectively, were not

251  significantly different.

252  Standard deviations are within

253  the upper range of the

254  standard deviations reported

255  in the literature for the here

256  applied 3D local method [16,

257  42]. Contact angles are

258  generally expected to be



Figure 4. Hydrogen drainage capillary pressure curve for the two Clashach sandstone core plugs of our study as compared to studies by Yekta et al. [29] and Boon & Hajibeygi [30] on Vosges and Berea sandstones, respectively.

259  larger for imbibition than for drainage [21]. The here observed a higher drainage contact angle

260  may be an artefact caused by resolution limitation to our measurements.

261  Hydrogen/brine/Clashach sandstone contact angles after imbibition were 58° at all pore fluid

262  pressures (Fig. 2b), indicating a water-wet rock and, despite the significant cluster build-up at

263  7 MPa (Fig. 1e, 2b), wettability does not change with pore fluid pressure. These combined

264  findings are in line with $H_2$ cluster size distributions for the same experimental data [11], which
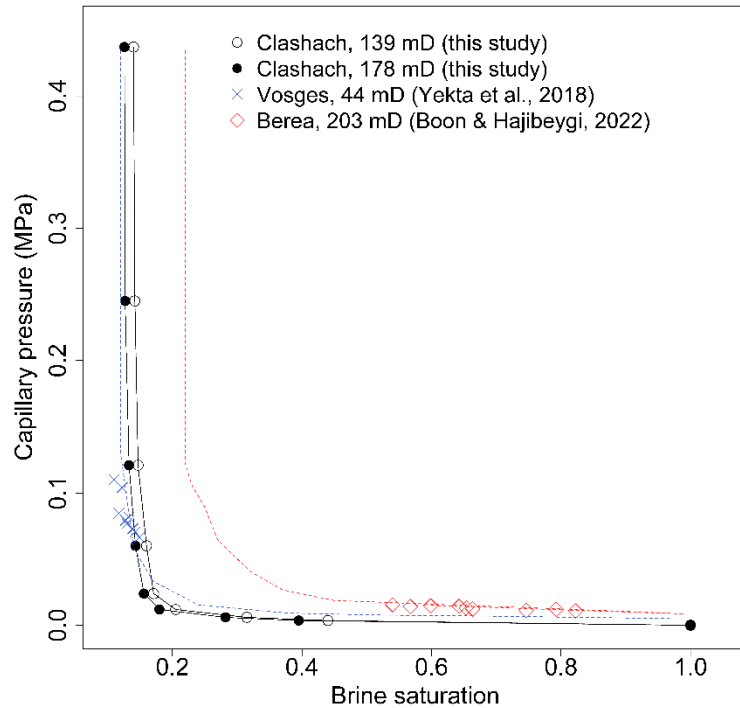
265 show an increase in the number of intermediate size clusters at 7 MPa, without shifting the

266 cluster distribution horizontally, suggesting no wettability change.

267 The amount of $H_2$ residual trapping is a function of 1) the contact angle, 2) the rock porosity

268 and rock pore morphology, 3) the initial $H_2$ saturation and connectivity, and 4) the $H_2$–brine

269 IFT. The IFT of $H_2$–brine decreases by 1% with pressure increases from 2 to 7 MPa (from

270 73.982 to 73.293 mN $m^{-1}$)[27] and is hence unlikely to impact residual trapping significantly.

271 Hence, with no changes in the IFT and in the contact angle (Fig. 2b), and no change in the rock

272 porosity and rock pore morphology due to the deployment of the same Clashach sandstone

273 sample in all experiments, increased trapping at 7 MPa can only be attributed to the decreased

274 $H_2$ connectivity during drainage. Noteworthily, a poorer initial connectivity of hydrogen was

275 not confirmed by the repetition of primary drainage at 7 MPa (Fig. 1f). It is possible, that some

276 salt precipitated during the experiments and blocked a pore throat which could have altered the

277 $H_2$ flow path, thereby leading to decreased initial connectivity and/or increased $H_2$ trapping

278 during imbibition. Salt precipitation is more pronounced at higher pressures as higher pressures

279 lead to increased drying of the brine by the injected gas [12]. The increased $H_2$ $S_{nwr}$ at 7 MPa

280 is subject to further investigations. Future work should target conducting repeated cyclic $H_2$

281 and brine injection experiments at 7 MPa pore fluid pressure and higher, as well as experiments

282 with $H_2$-saturated brine, to elucidate the reproducibility and any potential effect of gas

283 dissolution on our results.

284

285 *4.2 $N_2$-brine-Clashach sandstone contact angles*

286 Considering standard deviations of ~ 20% in our experiments, the $N_2$ contact angles for

287 drainage and imbibition were not significantly different. Further, $N_2$ contact angles were not

288 significantly different from $H_2$ contact angles (Figs. 2 and 3). In view of similar $S_{nwi}$ for $H_2$ and

289 $N_2$ (Fig. 1c,d, g), the similar $\theta_{receding}$ were expected. However, the $N_2$ $S_{nwr}$ was >20% greater

290  than for $H_2$ (Fig. 1c,d, g), so a lower gas wettability, i.e. lower $N_2$ $\theta_{advancing}$, was anticipated.

291  Because $N_2$ and $H_2$ experiments used the same rock sample, only differences in the contact

292  angle and/or differences in the IFT could have caused the higher $S_{nwr}$ for $N_2$. For any given

293  pressure, the IFT of $N_2$ is lower than for $H_2$ (SI Table 2), hence, according to theory, at similar

294  $\theta_{advancing}$, $N_2$ residual trapping should decrease relatively to $H_2$ residual trapping. The higher

295  $S_{nwr}$ of $N_2$ over $H_2$ is subject to further investigations.

296  Higher capillary trapping of $N_2$ over $H_2$ has been shown previously in connection to an almost

297  doubled $S_{nwi}$ of $N_2$ over $H_2$ ($\mu$CT method, Bentheimer sandstone, 1 MPa pressure and ambient

298  temperature) [32]. Here, the lower $S_{nwi}$ of $H_2$ over $N_2$ was suspected not to be caused by

299  differences in $\theta_{receding}$ but to arise from $H_2$ dissolution as well as channeling, driven by the lower

300  viscosity of $H_2$ compared to $N_2$ [32]. Our data do not confirm the observations of $H_2$ channeling

301  during drainage (Fig. 1, [11]). Residual $H_2$ was distributed mainly over one side of the rock

302  sample (Fig. 1a, b, c) which could indicate some preferentiality in the $H_2$ fluid flow during

303  imbibition.

304

305  *4.3 Relation to other work*

306  *4.3.1 Hydrogen*

307  To date, ten studies either measured or derived $H_2$/brine/sandstone or pure quartz contact

308  angles. While there is general consensus in the literature that unaged $H_2$/brine/quartz or

309  sandstone systems are water-wet, contact angles vary with rock type, sample preparation and

310  measurement methodology as well as experimental condition. Because the in-situ contact angle

311  method captures the effects of local pore geometry and surface roughness it provides a more

312  accurate representation of the fluid interaction in porous media than contact angle data from

313  the tilted plate method or the captive bubble method [27]. Four studies, all conducted on

314  Bentheimer sandstone, applied the same in-situ contact angle measurement methodology as in

16

315 this work: Higgs et al. measured $\theta_{advancing}$ of 59.8° and 57° at ambient temperature and 0.4 MPa

316 and 2.1 MPa, respectively [27, 48]. Jangda et al. [16] reported $\theta_{advancing}$ between 52.7° - 53.7°

317 at 10 MPa and 323 K. Zhang et al. [32] reported $\theta_{advancing}$ of ~57° at ambient temperature and 1

318 MPa. All results are very close to our $\theta_{advancing}$ of 58° at 2-7 MPa and ambient temperature. The

319 Bentheimer sandstone is more porous than Clashach (23% porosity vs. 12.5-13.6% porosity,

320 respectively [11, 16, 48]) and has ~ 4 % less quartz than Clashach, with correspondingly

321 increased clay and feldspar fractions [49].

322 Previous reports of $\theta_{receding}$ in Bentheimer sandstone range from 44° to ~75° (1- 2.1 MPa,

323 ambient temperature) [32, 48], a range that brackets the here measured 61°.

324 The captive bubble method, applied to Bentheimer and Berea sandstones, yielded lower

325 $H_2$/brine contact angles (25°-45°) [27, 28] than the in-situ method but coincided with this study

326 in that there was no correlation between contact angle and pressure (measured over a range of

327 6.9-20.7 MPa). The captive bubble method was also recently used to measure

328 $H_2$/brine/carbonate rock contact angles, again with no effect of increasing pressure and

329 temperature on the contact angle [50]. However, when applied to quartz samples aged in

330 organic acids, increasing contact angles with increasing pressure and temperature were

331 reported [51].

332 Using the tilted-plate method on pure quartz, advancing contact angles of 40.8° have been

333 reported (temp: 323 K, pressure: 25 MPa) [52] and increases in contact angles from 0° to a

334 maximum of ~50° were observed at increases from 296 K and 0.1 MPa to 343 K and 25 MPa

335 [31]. The authors argued that the reported trend in contact angles is caused by the increasing

336 intermolecular quartz–gas interactions with increasing molecular gas density at increased

337 pressure [31].

338 Calculations of $H_2$/brine contact angles from $P_c$ curves for Berea and Vosges sandstone

339 yielded 45° [30] and 21.6° to 34.9° [29], respectively, depending on the experimental condition

340    (Berea: 10 MPa and 219K; Vosges sandstone, 5 MPa and 293K, and 10 MPa and 318K,

341    respectively).

342    The $P_{cH2}$ curve for Clashach was similar to the Vosges sandstone $P_c$ curve from Yekta et al.

343    [53] (derived using the results from both of the tested pressure and temperature conditions; Fig.

344    4), despite the significantly lower relative permeability of the Vosges sandstone. The $P_c$ for

345    Berea sandstone from Boon & Hajibeygi [30] was higher than for Clashach and Vosges

346    sandstone (Fig. 4). The saturations for the $P_c$ measurements in Yekta et al. [53] and Boon &

347    Hajibeygi [30] cover a small range, resulting in a higher uncertainty in the fit of the mercury

348    injection capillary pressure data.

349

350    *4.3.2 Nitrogen*

351    Studies on $N_2$/brine/rock contact angles are scarce. Reported effective $N_2$ contact angles

352    range from 30° on quartz (captive bubble method, 5 MPa and 313 K) [54] to 25-47° in illite

353    and kaolinite (tilted plate method, 5-10 MPa and 60°C) [55, 56], with 3-6° higher $\theta_{receding}$ than

354    $\theta_{advancing}$ [56], and are larger than $H_2$ contact angles of ~10-20° on the same minerals [55]. A

355    stronger gas-wetting behavior of $N_2$ relative to $H_2$ [55] was indicated by our experiments but

356    not statistically significant. Higher wettability of $N_2$ over $H_2$ would be favorable for gas

357    separation during production if $N_2$ is used as a cushion gas.

358    Our results are close to mean in-situ $N_2$ contact angles of ~71° at 1 MPa and 298 K in

359    Bentheimer sandstone [32] and to ~69° on smooth silicon in water at 5 MPa and 296 K [57].

360    The observed differences between $\theta_{advancing}$ and $\theta_{receding}$ correspond well with previous reports

361    from air-water systems [58]. Our results are significantly higher than 40-60 manually measured

362    in-situ $N_2$ $\theta_{receding}$ and $\theta_{advancing}$ of 34°±6° and 46°±6°, respectively, in Berea sandstone at 5.5

363    MPa and ambient temperature [24]. Considering 2800 times more contact angles measured in

364    this study as well as the use of an automated approach to remove potential selection bias that

365 might exist in manual methods, one may suspect that our study resulted in more representative

366 answer.

367

368 4. CONCLUSION

369    In this work, in-situ contact angles for the $H_2$/brine/Clashach sandstone system were

370 quantified at 2-7 MPa pore fluid pressure to identify any control of wettability on $S_{nwr}$.

371 Measurements of $N_2$/brine/Clashach sandstone contact angles at 5 MPa and $N_2$ $P_c$ with varying

372 brine saturations, enabled the novel calculation of the $P_{cH2}$ curve.

373    Contrary to our hypothesis, the average receding contact angles did not decrease with

374 increasing pore fluid pressure but showed a mean of 58° at all pressures, suggesting that

375 observed higher $S_{nwr}$ at 7 MPa were not caused by wettability changes. Instead, the elevated

376 $S_{nwr}$ at increased pressure was likely instigated by a decreased connectivity after drainage,

377 however decreased connectivity was not confirmed by a repetition experiment. More

378 experiments at 7 MPa and higher pressure will need to be undertaken to confirm the trend in

379 $S_{nwr}$ with pressure. Comparison with other studies showed good alignment with other *in-situ*

380 $H_2$ contact angle measurements in sandstone but revealed that measurements in artificial

381 systems significantly underestimate the $H_2$/brine/sandstone contact angle. Overall, this study

382 and other emerging research suggests that for contact angles around 58°-70°, wettability may

383 not always be the main control for the $H_2$ saturation in the pore space but that $H_2$ dissolution

384 and channeling events may significantly affect those parameters.

385    Average $N_2$/brine/Clashach sandstone contact angles at 5 MPa were 66° and 62° during

386 drainage and imbibition, respectively, and not significantly different from $H_2$ contact angles.

387 This matched a similar $S_{nwi}$ for $N_2$ and $H_2$, yet could not explain a 20% higher $S_{nwr}$ relative to

388 $H_2$.

19

389　The $P_{cH2}$ plays a noteworthy role in understanding how $H_2$ interacts within porous media.

390　When $H_2$ encounters a rock's pore spaces, this parameter helps quantify the onset of its

391　movement and displacement of the resident fluid, like brine. The novel $P_{cH2}$ for Clashach

392　sandstone in our experiments was determined with a previously unseen precision. At an

393　irreducible water saturation of 13.6-14.0% the $P_{cH2}$ was 0.43 MPa. The relevance of such data

394　extends to areas such as underground $H_2$ storage, where understanding these interactions can

395　influence storage designs and predictions.

396

397　ASSOCIATED CONTENT

398　Supporting information: TEXT S1 ´Measurements required for the calculation of the Hydrogen

399　capillary pressure´ which comprises the base results used to create Figure 4 (SI Table 2).

400

401

402　AUTHOR INFORMATION

403　**Corresponding Author**

404　Katriona Edlmann. Email: katriona.edlmann@ed.ac.uk

405

406　**Author Contributions**

407　　The experimental kit was built by Butler and Thaysen. Hydrogen and brine displacement

408　experiments were carried out by Thaysen and Butler. Image reconstruction and tomographic

409　analysis was carried out by Thaysen, Jangda, Menke and Singh. The calculation of the

410　hydrogen capillary pressure with varying brine saturations was by Hassanpouryouzband.

411　Interpretation of the results was by Thaysen, Butler, Heinemann and Hassanpouryouzband.

412　The manuscript was written by Thaysen, with contributions and review from Butler,

413　Hassanpouryouzband, Edlmann, Heinemann, Jangda, Menke and Singh. All authors have

414　given approval to the final version of the manuscript.

ABBREVIATIONS

$H_2$= hydrogen, $N_2$= nitrogen, $N_c$= capillary number, $P_c$= capillary pressure, $P_{cH2}$= hydrogen capillary pressure, $S_{nwi}$ = initial saturation, $S_{nwr}$= residual saturation, $\theta_{advancing}$= imbibition contact angle, $\theta_{receding}$= drainage contact angle.

REFERENCES

1.  IPCC, IPCC report Global Warming of 1.5 C: Summary for Policymakers. 2018

2.  Organization, W.H., *Fact sheets on climate change and health and biodiversity and health* 2022.

3.  Thaysen, E.M., et al., *Effect of dissolved $H_2SO_4$ on the interaction between $CO_2$-rich brine solutions and limestone, sandstone and marl.* Chem Geol, 2017. **450**: p. 31-43.

438    4.    Thaysen, E.M., et al., *Effects of lime and concrete waste on vadose zone carbon cycling.*

439    Vadose Zone J, 2014. **13**(11): p. 1-11.

440    5.    Snæbjörnsdóttir, S.O., et al., *Carbon dioxide storage through mineral carbonation.* Nat

441    Rev Earth Environ, 2020. **1**: p. 90-102.

442    6.    Beckingham, L.E. and L. Winningham, *Critical knowledge gaps for understanding*

443    *water-rock-working phase interactions for compressed energy storage in porous formations.*

444    ACS Sustain Chem Eng, 2020. **8**(1): p. 2-11.

445    7.    Heinemann, N., et al., *Hydrogen storage in porous geological formations - onshore*

446    *play opportunities in the Midland Valley (Scotland, UK).* Int J Hydrog Energy, 2018. **43**(45):

447    p. 20861-20874.

448    8.    Kharel, S. and B. Shabani, *Hydrogen as a long-term large-scale energy storage*

449    *solution to support renewables.* Energies, 2018. **11**(10): p. 1-17.

450    9.    Heinemann, N., et al., *Enabling large-scale hydrogen storage in porous media: the*

451    *scientific challenges.* Energy Environ Sci, 2021. **14**: p. 853-864.

452    10.    Matos, C.R., J.F. Carneiro, and P.P. Silva, *Overview of large-scale underground energy*

453    *storage technologies for integration of renewable energies and criteria for reservoir*

454    *identification.* J. Energy Storage, 2019. **21**: p. 241-258.

455    11.    Thaysen, E.M., et al., *Pore-scale imaging of hydrogen displacement and trapping in*

456    *porous media.* Int J Hydrog Energy, 2023. **48**(8): p. 3091-3106.

457    12.    Hassanpouryouzband, A., et al., *Geological Hydrogen Storage: Geochemical*

458    *Reactivity of Hydrogen with Sandstone Reservoirs.* ACS Energy Lett, 2022. **7**: p. 2203-2210.

459  13.  Aftab, A., Hassanpouryouzband, A., Martin, A., Kendrick, J. E., Thaysen, E.M.,

460  Heinemann, N., Utley, J., Wilkinson, M., Haszeldine, R. S., Edlmann, K., *Geochemical*

461  *Integrity of Wellbore Cements during Geological Hydrogen Storage.* Environ Sci Technol Lett,

462  2023. **in press**.

463  14.  Thaysen, E.M., et al., *Estimating microbial growth and hydrogen consumption in*

464  *hydrogen storage in porous media.* Renew Sustain Energ Rev, 2021. **151**(111481): p. 1-15.

465  15.  Heinemann, N., et al., *Hydrogen storage in saline aquifers: The role of cushion gas for*

466  *injection and production.* Int J Hydrog Energy, 2021. **46**: p. 39284-39296.

467  16.  Jangda, Z., et al., *Pore-Scale Visualization of Hydrogen Storage in a Sandstone at*

468  *Subsurface Pressure and Temperature Conditions: Trapping, Dissolution and Wettability.* J

469  Colloid Interf Sci, 2022. **629**(Part B): p. 316-325.

470  17.  Rezaei, A., et al., *Relative permeability of hydrogen and aqueous brines in sandstones*

471  *and carbonates at reservoir conditions.* Geophys Res Lett, 2022.

472  18.  Thaysen, E.M., Armitage, T., Slabon, L., Hassanpouryouzband, A., Edlmann, K.,

473  *Microbial risk assessment for underground hydrogen storage in porous rocks* Fuel, 2023. **in**

474  **press**.

475  19.  Yekta, A.E., M. Pichavant, and P. Audigane, *Evaluation of geochemical reactivity of*

476  *hydrogen in sandstone: Application to geological storage.* J Appl Geochem, 2018. **95**: p. 182-

477  194.

478  20.  Heinemann, N., Wilinson, M., Adie, K., Edlmann,K., Thaysen,

479  E.M.,Hassanpouryouzvband, A., Haszeldine, R.S., *Cushion Gas in Hydrogen Storage—A*

480  *Costly CAPEX or a Valuable Resource for Energy Crises?* Hydrogen, 2022. **3**(4): p. 550-563.

481     21.    Blunt, M.J., *Multiphase flow in permeable media. A Pore-scale perspective.* 2017,

482     Cambridge, United Kingdom: Cambridge University Press.

483     22.    Lysyy, M., G. Ersland, and M. Fernø, *Pore-scale dynamics for underground porous*

484     *media hydrogen storage.* Adv Water Resour, 2022. **163**(104167): p. 1-13.

485     23.    Morrow, N.R., *Wettability and its effect on oil recovery.* J Pet Technol, 1990. **42**(12):

486     p. 1476–1484.

487     24.    Khishvand, M., A.H. Alizadeh, and M. Piri, *In-situ characterization of wettability and*

488     *pore-scale displacements during two- and three-phase flow in natural porous media.* Adv

489     Water Resour, 2016. **97**: p. 270-298.

490     25.    Scanziani, A., et al., *Automatic method for estimation of in situ effective contact angle*

491     *from X-ray micro tomography images of two-phase flow in porous media.* Journal of Colloid

492     and Interface Science, 2017. **496**: p. 52-59.

493     26.    Muhammed, N.S., B. Haq, and D.A. Al Shehri, *Hydrogen storage in depleted gas*

494     *reservoirs using nitrogen cushion gas: A contact angle and surface tension study.* International

495     Journal of Hydrogen Energy, 2023.

496     27.    Higgs, S., et al., *In-situ hydrogen wettability characterisation for underground*

497     *hydrogen storage.* Int J Hydrog Energy, 2021. **47**(26): p. 13062-13075.

498     28.    Hashemi, L., et al., *Contact angle measurement for hydrogen/brine/sandstone system*

499     *using captive-bubble method relevant for underground hydrogen storage.* Adv Water Resour,

500     2021. **154**(103964): p. 1-13.

501   29.   Yekta, A.E., et al., *Determination of Hydrogen-Water Relative Permeability and*
502   *Capillary Pressure in Sandstone: Application to Underground Hydrogen Injection in*
503   *Sedimentary Formations.* Transport in Porous Media, 2018. **122**(2): p. 333-356.

504   30.   Boon, M. and H. Hajibeygi, *Experimental characterization of H2/water multiphase*
505   *flow in heterogeneous sandstone rock at the core scale relevant for underground hydrogen*
506   *storage (UHS).* Nat Sci Rep, 2022. **12**(14604): p. 1-11.

507   31.   Iglauer, S., A. Muhammad, and A. Keshavarz, *Hydrogen wettability of sandstone*
508   *reservoirs: implications for hydrogen geo-storage.* Geophys Res Lett, 2020. **48**(3): p. 1-5.

509   32.   Zhang, Y., Bijeljic, B., Gao, Y., Goodarzi, S., Foroughi, S., Blunt, M.J., *Pore-Scale*
510   *Observations of Hydrogen Trapping and Migration in Porous Rock: Demonstrating the Effect*
511   *of Ostwald Ripening.* Geophys Res Lett, 2023. **50**(e2022GL102383).

512   33.   Lysyy, M., et al., *Hydrogen relative permeability hysteresis in underground storage.*
513   Geophys Res Lett, 2022. **49**: p. 1-8.

514   34.   Al-Yaseri, A., et al., *Initial and residual trapping of hydrogen and nitrogen in*
515   *Fontainebleau sandstone using nuclear magnetic resonance core flooding.* Int J Hydrog
516   Energy, 2022. **47**(53): p. 22482-22494.

517   35.   Iglauer, S., et al., *Comparison of residual oil cluster size distribution, morphology and*
518   *saturation in oil-wet and water-wet sandstone.* Journal of Colloid and Interface Science, 2012.
519   **375**: p. 187-192.

520   36.   Iglauer, S., A. Paluszny, and M.J. Blunt, *Simultaneous oil recovery and residual gas*
521   *storage: A pore-level analysis using in situ X-ray micro-tomography.* Fuel, 2013. **103**: p. 905-
522   914.

523   37.   Pentland, C.H., et al., *Capillary trapping in water-wet sandstones: coreflooding*
524   *experiments and pore-network modeling*, in *SPE International* 2010, Society of Petroleum
525   Engineers Florence, Italy

526   38.   Yusibani, E., et al., *A capillary tube viscometer designed for measurements of hydrogen*
527   *gas viscosity at high pressure and high temperature.* International Journal of Thermophysics,
528   2011. **32**(6): p. 1111-1124.

529   39.   Chow, Y.T.F., G.C. Maitland, and J.P.M. Trusler, *Interfacial tensions of (H2O + H-2)*
530   *and (H2O + CO2 + H-2) systems at temperatures of (298-448) K and pressures up to 45 MPa.*
531   Fluid Phase Equilibria, 2018. **475**: p. 37-44.

532   40.   Chow, Y.T.F., G.C. Maitland, and J.P.M. Trusler, *Erratum to "Interfacial tensions of*
533   *(H2O + H-2) and (H2O + CO2 + H-2) systems at temperatures of (298-448) K and pressures*
534   *up to 45 MPa".* Fluid Phase Equilibria, 2020. **503**(112315): p. 1.

535   41.   Niu, B., A. Al-Menhali, and S.C. Krevor, *The impact of reservoir conditions on the*
536   *residual trapping of carbon dioxide in Berea sandstone.* Water Resour Res, 2015. **51**(4): p.
537   2009-2029.

538   42.   AlRatrout, A., Raeini, A. Q., Bijeljic, B. & Blunt, M. J., *Automatic measurement of*
539   *contact angle in pore-space images.* Advances in Water Resources, 2017. **109**: p. 158–169.

540   43.   Hassler, G.L., Brunner. E., *Measurement of capillary pressures in small core samples.*
541   Transactions of the AIME, 1945. **160**(01): p. 114-123.

542   44.   Hassanpouryouzband, A., et al., *Offshore Geological Storage of Hydrogen: Is This Our*
543   *Best Option to Achieve Net-Zero?* ACS Energy Lett, 2021. **6**(6): p. 2181–2186.

544    45.    Danesh, A., *PVT and Phase Behaviour Of Petroleum Reservoir Fluids*. Vol. 47. 1998,

545    Department of Petroleum Engineering, Heriot Watt University, Edinburgh, Scotland: Elsevier.

546    46.    Kalantari Meybodi, M., A. Daryasafar, and M. Karimi, *Determination of hydrocarbon-*

547    *water interfacial tension using a new empirical correlation.* Fluid Phase Equilibria, 2016. **415**:

548    p. 42-50.

549    47.    Singh, K., et al., *Time-resolved synchrotron X-ray micro-tomography datasets of*

550    *drainage and imbibition in carbonate rocks.* Scientific Data, 2018. **5**(1): p. 180265.

551    48.    Higgs, S., et al., *Direct measurement of hydrogen relative permeability hysteresis for*

552    *underground hydrogen storage.* International Journal of Hydrogen Energy, 2023.

553    49.    Peksa, A.E., Wolf, K. H. A. A., Zitha, P. L. J., *Bentheimer sandstone revisited*

554    *for experimental purposes.* Marine and Petroleum Geology, 2015. **67**: p. 701-719.

555    50.    Aghaei, H., Ahmed Al-Yaseri, A., Toorajipour, A., Shahsavani, B., Yekeen, N.,

556    Edlmann, K., *Host-rock and caprock wettability during hydrogen drainage:Implications of*

557    *hydrogen subsurface storage.* Fuel, 2023. **351**(129048).

558    51.    Esfandyari, H., et al., *Experimental evaluation of rock mineralogy on hydrogen-*

559    *wettability: Implications for hydrogen geo-storage.* J Energy Storage, 2022. **52**(104866): p. 1-

560    8.

561    52.    Ali, M., Jha, N.K., Al-Yaseri, A., Zhang, Y., Iglauer, S., Sarmadivaleh, M., *Hydrogen*

562    *wettability of quartz substrates exposed to organic acids; Implications for hydrogen geo-*

563    *storage in sandstone reservoirs.* Journal of Petroleum Science and Engineering, 2021.

564    **207**(109081).

565 53. Yekta, A.E., et al., *Determination of Hydrogen-Water Relative Permeability and*

566 *Capillary Pressure in Sandstone: Application to Underground Hydrogen Injection in*

567 *Sedimentary Formations.* Transport Porous Med, 2018. **122**(2): p. 333-356.

568 54. Mills, J., M. Riazi, and M. Sohrabi. *Wettability of common rock-forming minerlas in a*

569 *CO2-brine system at reservoir conditions*. in *International Symposium of the Society of Core*

570 *Analysts*. 2011.

571 55. Al-Yaseri, A., et al., *Hydrogen wettability of clays: Implications for underground*

572 *hydrogen storage.* Int J Hydrog Energy, 2021. **46**(69): p. 34356-34361.

573 56. Fauziah, C.A., et al., *Carbon Dioxide/Brine, Nitrogen/Brine, and Oil/Brine Wettability*

574 *ofMontmorillonite, Illite, and Kaolinite at Elevated Pressure andTemperature.* Energy Fuels,

575 2019. **33**: p. 441-448.

576 57. Song, J.-W. and L.-W. Fan, *Understanding the effects of pressure on the contact angle*

577 *of water on a silicon surface in nitrogen gas environment: Contrasts between low- and high-*

578 *temperature regimes*. Journal of Colloid and Interface Science, 2022. **607**: p. 1571-1579.

579 58. Behnoudfar, D., et al., *Contact angle hysteresis: A new paradigm?* Advances in Water

580 Resources, 2022. **161**: p. 104138.

581 59. Forbes, P.L., *Simple and Accurate Methods for Converting Centrifuge Data into*

582 *Drainage and Imbibition Capillary Pressure Curves.* The log Analyst, 1994. **35**(4): p. 31-53.

583

584    SUPPORTING INFORMATION

585

586    **TEXT S1 Measurements required for the calculation of the Hydrogen capillary pressure**

587    <u>Permeability to nitrogen</u>

588    Two fully dried Clashach sandstone plugs (length: 5.0 cm, diameter: 3.8 cm) were each

589    placed in a Hassler core holder (Standard Core Holder- HCH Series, Core Laboratories, UK),

590    maintaining a sleeve pressure of 2.76 MPa. Dry nitrogen was channeled through the core plug

591    at a consistent flow rate until the pressure readings were stable, and both the upstream and

592    downstream pressures were documented. The steady-state permeability to nitrogen at a low

593    mean pore pressure was determined using equation 1:

594    $$k_{air} = \frac{1000 \times Pa \times \mu_N \times q_N \times L}{(P_i - P_0)(P_i + P_0)/2 \times A}$$    *(1)*

595    where $k_{air}$ is the permeability (mD), $q_N$ is the flow rate of nitrogen at atmospheric pressure

596    (cm$^3$/s), $\mu_N$ is the viscosity of nitrogen (cP), $L$ is the length of core plug (cm), $A$ is the cross-

597    sectional area of core plug (cm$^2$), and $Pi$, $Po$ and $Pa$ are the upstream pressure, the downstream

598    pressure and the atmospheric pressure, respectively (all in atm).

599

600    <u>Helium Porosity and Grain Density</u>

601    The clean and dry plug samples were first weighed. Subsequently, their grain volumes were

602    determined using a Pycnometer System (UltraPore$^{TM}$300, Anton-Paar ,USA). This automated

603    gas displacement pycnometer computes density and grain volume by assessing the pressure

604    variation of helium within a pre-calibrated volume that expands into a matrix cup housing the

605    plug sample. The system relies on computer-based processing for all pressure readings and

606    calculations, effectively minimizing potential transcription errors.

607     Each of the clean, dry samples was placed into a designated matrix cup connected to the

608     system. Helium, with a predetermined pressure sourced from a reference cell of known volume,

609     was expanded into the matrix cup, and the resultant pressure was recorded. Using Boyle's Law,

610     grain volumes were computed based on a modified version of the standard equations:

611     Boyle's Law calculation      $P_1V_1 = P_2V_2$                                 (2)

612     Grain volume calculation      $P_1V_{ref} = P_2 (V_{ref} + V_{matrix} - V_g - V_{disk})$            (3)

613     Therefore:

614     

$$V_g = ((V_{matrix} + V_{ref}) - (P_1/P_2 . V_{ref})) - V_{disk} \tag{4}$$

615     where $P_1$ and $P_2$ are the pressure of helium in the reference cell and after expansion into

616     matrix cup, respectively, $V_{ref}$ is the volume of the reference cell, $V_{matrix}$ is the volume of the

617     matrix cup, $V_g$ is the grain volume of the plug sample, and $V_{disk}$ is the disk volume added to cup

618     to reduce dead space. To determine the true grain volume, the volume of any mounting material

619     was accounted for and subtracted.

620     The system is equipped with a precision 0-1.37 MPa transducer. Its linearity and hysteresis

621     have an impressive accuracy, registering less than +/- 0.11% of full scale. To ensure its

622     precision, the system undergoes calibration twice daily using steel disks with known volumes.

623     These disks receive their calibration externally. The calibration correlation factor must

624     consistently fall within the range of 1.0000 +/- 0.0001 for validity. For enhanced accuracy,

625     beyond the regular calibrations, check plugs are measured roughly after every ten samples. At

626     the conclusion of each worksheet, at least one sample undergoes a double-check to ensure

627     consistency.

628     Grain density was derived from the grain volume and the dry weight of the sample.

629     Adjustments were made for the weight of any mounting material when necessary. Bulk volume

630  ($V_b$) was ascertained using mercury displacement. Subsequently, pore volume ($V_p$) and porosity

631  ($\phi$) were computed according to equations 5 and 6:

632  $$V_p = V_b - V_g \tag{5}$$

633  $$\phi = V_p / V_b \tag{6}$$

634

635  Table S1 shows the results of the $N_2$ permeability, the porosity and the grain density

636  measurements.

637

638  SI Table 1. Permeability and Porosity of Clashach core samples

| Plug | $K_{N2}$, millidarcies | Porosity, frac | Grain density, g/cc |
|------|------------------------|----------------|---------------------|
| 1    | 139                    | 0.130          | 2.64                |
| 2    | 178                    | 0.131          | 2.64                |

639

640

641  <u>Core Sample Saturation with 0.5 M Caesium Chloride</u>

642  The clean and dry Clashach sandstone plugs were first weighed. Subsequently, they were

643  placed inside a sealed container and subjected to evacuation for a period of 24 hours. After the

644  evacuation, the container was filled with the same brine that was utilized for the $H_2$ and brine

645  core-flood experiments (0.5 M CsCl). The brine was then pressurized to 13.8 MPa, and this

646  pressure was sustained for an additional 24 hours.

647  After the stipulated time, the brine pressure was gently released. The samples, now saturated

648  with brine, were extracted from the container and weighed. The difference in weight between

649 the dry and saturated samples serves as an indicator of the brine volume within each sample.

650 This value was collated with the pore volume deduced from helium injection.

651     In addition, every brine-saturated sample was weighed when submerged in the saturating

652 brine. Utilizing Archimedes' principle, a bulk volume was computed. Saturation porosity was

653 then determined using the derived saturation pore volume and the calculated Archimedes bulk

654 volume. This saturation porosity was subsequently compared to the porosity determined

655 through helium injection.

656

657 <u>Capillary Pressure Determination</u>

658     The Clashach sandstone plugs were pressure-saturated with 0.5 M CsCl, as detailed in section

659 2.3.3. Each plug was positioned in a rotor bucket equipped with a graduated receiving tube and

660 mounted onto the body of a high-speed centrifuge. The centrifuge employed was an

661 ACES200—an automated, camera-enabled system that incorporated a modified Beckman

662 L100 Optima centrifuge with its associated control software.

663     The receiving tube and the void around each sample were filled with the displacing phase,

664 which in this context, is air. The rotor can accommodate up to three 1.5-inch diameter plugs

665 simultaneously. In scenarios where brine saturation diminishes (like in drainage, which is the

666 case here), the receiving tubes are strategically positioned farther from the rotation's center than

667 the plugs, ensuring efficient brine collection.

668     The rotor, loaded with the plugs, was subjected to varied rotation speeds, ranging between

669 800 to 7500 rpm. These speeds were chosen to generate equivalent capillary pressures ($Pc$)

670 within a spectrum of approximately 0.02 MPa to around 2.07 MPa, especially for an air-

671 displacing-brine mechanism. While the rotor was spinning, a stroboscopic light illuminated the

672 receiving tube to determine the volume of brine displaced from each plug. Readings can be

673　taken either manually or captured with a camera. In this case, we recorded the readings

674　manually. Every core plug was retained at each specific capillary pressure until it reached

675　equilibration for the given pressure. After a span ranging from 24 to 48 hours, equilibration

676　was confirmed if the fluid volume displaced from each core plug remained unaltered for a

677　consecutive 4-hour period. The rotor bucket assemblies' weights were recorded before and [43]

678　post-test to identify any potential evaporative losses. The volumes of brine displaced, plug pore

679　volumes, and the respective capillary pressures derived from test parameters were utilized to

680　deduce capillary pressure and saturation data. Further details about the method can be found

681　elsewhere [43].

682

683　<u>Calculation of Centrifuge Air-Brine Capillary Pressure from Brine Displacement Data</u>

684　Average brine saturations were adjusted for capillary end effects, and the end-face brine

685　saturations were derived using Pierre Forbes' methodology [59]. Capillary Pressure ($P_c$) was

686　deduced from the rotation rates via equation 7:

687
$$P_c = 1.578 \text{x} 10^{-7} \times (\rho_b - \rho_{air}) \times (R - L/2) \times L \times RPM^2 \tag{7}$$

688　where $\rho_b$ is density of brine (1.06 g/cm$^3$), $\rho_{air}$ is the density of air (0.0012 g/cm$^3$), $R$ is the

689　distance from centre of rotation to outer face of the core plug in cm, $L$ is the length of core plug

690　in cm, and $RPM$ are revolutions per minute. From the above relationship it can be seen that the

691　capillary pressure generated for each sample at each spin speed can be different due any

692　differences in plug length.

693　The average brine saturation, $Sw_{avg}$, is determined using equation 8:

694

$$Sw_{avg} = \frac{Vp - V_{displaced}}{Vp} \qquad (8)$$

695      where $Vp$ is the pore volume in $cm^3$ and $V_{displaced}$ is the volume of displaced fluid in $cm^3$.

696      Capillary pressure curves for each sample were derived using Forbes' equations [59]. The

697      results, presented in both tabular and graphical formats, include inlet end-face brine saturations

698    SI Table 2. Parameters required for calculation of the $H_2$ capillary pressure using the $N_2$ capillary pressure data. $P_c$= capillary pressure, $\psi$=

699    conversion factor.

| $N_2$ $P_c$ (MPa) | Brine Sat. Sample 1 | Brine Sat. Sample 2 | Density $N_2$ (kg/m³) | Density $H_2$ (kg/m³) | Density 0.5 M CsCl (kg/m³) | IFT $N_2$ (mlN/m) | IFT $H_2$ (mlN/m) | Wettability $N_2$ (Cos(θ)) | Wettability $H_2$ (Cos(θ)) | $N_2$/Brine density difference | $H_2$/Brine density difference | Density Difference Ratio | IFT Ratio | Wetta bility ratio | ψ | $H_2$ $P_c$ (MPa) |
|---|---|---|---|---|---|---|---|---|---|---|---|---|---|---|---|---|
| 0 | 1 | 1 | 0 | 0 | 0 | 0 | 0 | 0 | 0 | 0 | 0 | 0 | | 0 | 0 | 0 |
| 0.003 | 0.44 | 0.395 | 0.237794532 | 0.017106 | 1,057.80 | 75.846 | 75.89 | 0.406737 | 0.484809 | 1057.562 | 1057.783 | 0.999791 | 1.00058 | 1.19195 | 1.1924 | 0.0035772 |
| 0.005 | 0.315 | 0.282 | 0.3963429 | 0.028508 | 1,057.81 | 75.812 | 75.887 | 0.406737 | 0.484809 | 1057.414 | 1057.781 | 0.999652 | 1.000989 | 1.19195 | 1.1927 | 0.0059636 |
| 0.01 | 0.205 | 0.18 | 0.79274184 | 0.057004 | 1,057.83 | 75.725 | 75.882 | 0.406737 | 0.484809 | 1057.037 | 1057.773 | 0.999304 | 1.002073 | 1.19195 | 1.1936 | 0.0119359 |
| 0.02 | 0.171 | 0.156 | 1.58573586 | 0.113962 | 1,057.85 | 75.552 | 75.871 | 0.406737 | 0.484809 | 1056.264 | 1057.736 | 0.998609 | 1.004222 | 1.19195 | 1.1953 | 0.0239063 |
| 0.05 | 0.16 | 0.143 | 3.966231 | 0.284558 | 1,057.94 | 75.04 | 75.837 | 0.406737 | 0.484809 | 1053.974 | 1057.655 | 0.996519 | 1.010621 | 1.19195 | 1.2004 | 0.0600208 |
| 0.1 | 0.147 | 0.133 | 7.9383462 | 0.567948 | 1,058.08 | 74.204 | 75.782 | 0.406737 | 0.484809 | 1050.142 | 1057.512 | 0.99303 | 1.021266 | 1.19195 | 1.2088 | 0.1208813 |
| 0.2 | 0.142 | 0.127 | 15.8982678 | 1.131278 | 1,058.37 | 72.598 | 75.672 | 0.406737 | 0.484809 | 1042.472 | 1057.239 | 0.986032 | 1.042343 | 1.19195 | 1.2251 | 0.2450133 |
| 0.35 | 0.14 | 0.126 | 27.8656098 | 1.967676 | 1,058.80 | 70.347 | 75.511 | 0.406737 | 0.484809 | 1030.934 | 1056.832 | 0.975495 | 1.073408 | 1.19195 | 1.2481 | 0.4368331 |

700

701